Seismic performance of moment connections in steel moment frames with HSS columns

Eduardo Nuñez[*1], Ronald Torres[2] and Ricardo Herrera[1]

[1]*Department of Civil Engineering, University of Chile, Av. Blanco Encalada 2002, Piso 4, 8370449 Santiago, Chile*
[2]*Materials and Structural Models Institute, Faculty of Engineering, Universidad Central de Venezuela, Caracas, Venezuela*

Abstract. The use of Hollow Structural Sections (HSS) provides an alternative for steel buildings in seismic zones, with the advantage over WF columns that the HSS columns have similar resistance along both axes and enhanced performance under flexure, compression and torsion with respect to other columns sections. The HSS columns have shown satisfactory performance under seismic loads, such as observed in buildings with steel moment frames in the Honshu earthquake (2011). The purpose of this research is to propose a new moment connection, EP-HSS ("End-plate to Hollow Structural Section"), using a wide flange beam and HSS column where the end plate falls outside the range of prequalification established in the ANSI/AISC 358-10 Specification, as an alternative to the traditional configuration of steel moment frames established in current codes. The connection was researched through analytical, numerical (FEM), and experimental studies. The results showed that the EP-HSS allowed the development of inelastic action on the beam only, avoiding stress concentrations in the column and developing significant energy dissipation. The experiments followed the qualification protocols established in the ANSI/AISC 341-10 Specification satisfying the required performance for highly ductile connections in seismic zones, thereby ensuring satisfactory performance under seismic actions without brittle failure mechanisms.

Keywords: ductility; performance; bolted connection; end-plate connection; hollow structural sections; moment connections; finite element method; steel structure; yield line; seismic design

1. Introduction

The Northridge (1994) and Kobe (1995) earthquakes showed deficiencies in the seismic performance of steel buildings, mainly in the behavior of their connections, initiating a search for new alternatives in configurations of steel structural systems and connections with capacity to achieve an acceptable level of performance. A large number of beam-column connections in more than 500 buildings showed local buckling in column flange and web, bolts fracture, welding fracture, and stress concentration in welding zones. The causes of the observed damage were deficient welding inspection and design, insufficient width-to-thickness ratios, and strength significantly larger than nominal strength on materials, showing that the concept of ductile behavior of steel moment frames was incompletely considered.

One of the most significant research efforts in the United States of America was the SAC project, conducted by the Applied Technology Council (ATC), the Consortium of Universities for Research in Earthquake Engineering (CUREE), and the Structural Engineers Association of California. This project resulted in the publication of a series of FEMA reports, FEMA (2000a) and FEMA (2000b), which presented more than 9 connections alternative to the pre-Northridge welded, unreinforced

flange (WUF) moment connection, showing better behavior in terms of stiffness and strength. Later, some of these connections were introduced in ANSI/AISC 358-10 (2010). However, out of eight connections for use in seismic design of steel moment frames, only a proprietary connection could be used with HSS columns, but only if it was a concrete filled column, where the beams were connected to the column with patented brackets. The Honshu (2011) earthquake showed that steel moment frames with HSS columns had satisfactory performance under seismic loads. Therefore, there is a need for additional research on moment connections between WF beams and HSS columns. Currently, the research has mainly focused on welded connections between WF beam to HSS column, HSS beam to HSS column, and WF beam to WF column (welded and bolted for this type). Some of these investigations are described below.

The response of end plate connections can be characterized using T shaped components. Swanson and León (2000), conducted a detailed study on T-stub connections. They performed numerous bolt tests, finding an overstrength of up to 43% and allowing the characterization of the behavior of bolts and the flexibility introduced by all the parts in the T-stub connection. Ataollahi and Banan (2016) studied a new steel moment connection with two concepts: (i) strengthening the connection (bolted T-stub connection) and (ii) weakening the beam ends (reduce beam section). The results show that moment capacity and dissipated energy of the new proposed connection is the same as those computed for a T-stub

---

connection and higher than corresponding values for an RBS connection. Murray and Sumner (2004) developed a design guide for end-plate moment connections between WF beams and WF columns, under wind and seismic loads. Based on numerous investigations, they established a capacity design methodology that aimed for the connection failure to be governed by ductile failure mechanisms, thereby preventing the manifestation of brittle failure mechanisms. The method considered the over strength of material and the strong column-weak beam criteria to ensure the formation of plastic hinges in the beams before than in the columns. In addition, Seek and Murray (2008) studied experimentally the effect of the concrete slab on the end-plate moment connection response, finding that the behavior of the connection depends on the presence of a gap between the slab and the connection. This separation ensures the adequate performance of the connection under seismic actions. All these studies were conducted using connections to the column's strong axes. The performance of a newly generated steel connection known as SidePlate moment connection for seismic loading and progressive collapse phenomenon has been studied by Faridmehr *et al.* (2015). The test results indicated that this type of connection had strength, stiffness and ductility to be categorized as a rigid, full-strength and ductile connection. Respect to connections to the column's weak axes, is known that traditional beam connections to the minor axis of a column have relatively low strength and stiffness. In this sense, Thair *et al.* (2014) conducted an experimental research with modified detail, using a plate welded between the toes of the column flange referred to as a toe plate connection. The results show a significant increase in both moment resistance and initial stiffness for this connection detail compared with connections made directly to the column web. Regarding the use of HSS members, Fadden (2013), Fadden and McCormick (2014a) and Fadden and McCormick (2014b), studied the cyclic response of HSS-to-HSS moment connections under seismic loads, proposing a welded connection incorporating plates that allowed an enhanced performance in terms of energy dissipation in the beam and the connection. This connection, however, was fully welded, requiring the use of field welding. Saleh *et al.* (2016) proposed a new connection with Reduced Beam Section (RBS) connection, called Tubular Web RBS connection (TW-RBS), where the obtained results indicated that TW-RBS reduces contribution of the beam web to the whole moment strength and creates a ductile fuse far from components of the beam-to-column connection. Similarly, Gholami *et al.* (2013) studied the behavior of welded connections between WF beam and Box Section columns, which required the addition of plates in the flanges and the web of the beam and field welding.

Recently, Yang *et al.* (2016) conducted an investigation to characterize the behavior of the proprietary "ConXL" connection using finite element method, when used in both directions in a joint. The study considered concrete filled and hollow columns. The results showed that this configuration could meet ductile failure mechanism as contemplated in the ANSI/AISC 358-10 (2010). Additionally, various ConXL connection joint configurations without concrete filling in the column showed beam hinging as failure mode when the axial load level in the column was not too high (less than 0.4 the capacity of the column). However, the failure mode can become a mixed beam–column hinge failure mechanism or even column hinge mechanism with an increase in the axial load level. In this topic, Esfandyary *et al.* (2015) studied to the hysteretic behavior of concrete filled steel tubular (CFT) column to I-beam connections. Following the verification of the numerical results against the available experimental tests, the finite element method (FEM) analysis was implemented to evaluate the effects of different parameters including the column axial load, beam lateral support, shape and arrangement of stiffeners, stiffness of T-stiffeners, and the number of shear stiffeners. It was shown that external T-stiffeners combined with internal shear stiffeners play an important role in the hysteretic performance of CFT columns to I-beam connections. These results were take account in external stiffeners design in this research wich will be shown in successive sections. Likewise, Čermelj and Beg (2014) and Čermelj *et al.* (2016), conducted a study using numerical models calibrated with data from prior testing between WF beam to Box Section column connection with welded plates that reinforce the connection. They studied the influence of complete joint penetration welds, achieving acceptable performance in those connections that use field welded CJP welds.

Field welding is a practice that is discouraged in many countries, particularly under cyclic or seismic loading. Therefore, it is necessary to develop a beam-column connection between WF beams and HSS columns in steel moment frames for building structures under seismic loads that does not require welding in the field. This paper describes the research conducted in such a connection, including analytical, numerical (FEM), and experimental studies and the development of a design procedure. The connection can be used for high seismicity zones, eliminating the need of field welding.

2. Description of EP-HSS moment connection

The EP-HSS (End Plate to Hollow Structural Section) connection is a new alternative for moment connections in Steel Moment Frames with Wide Flange beams and HSS columns. The beam end plates are connected by high strength bolts to a similar plate connected through external diaphragms to the HSS column (see Fig. 1).

A combination of fillet and complete joint penetration welds is used between plates to column and end plates respectively. This configuration simplifies the erection process in the field, because the beams are bolted on site, rather than welded, avoiding field welding and minimizing complications associated with the assembly and inspection. Shop-welded beam and column assemblies arrive ready for erection at the job site, providing a safer structural steel construction environment. In addition, the connection can be easily adapted for joints with up to 4 beams framing into the column in two perpendicular directions.

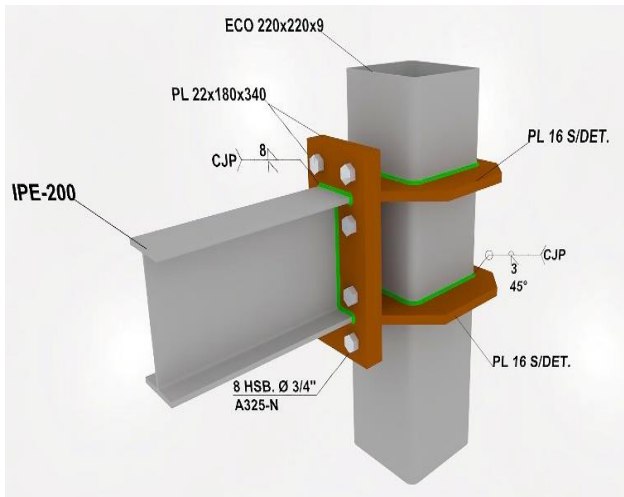The design process of the connection starts by

Fig. 1 View of EP-HSS Moment Connection

ANSI/AISC 358-10 (2010) and the proposed new expression will be derived and compared. The method of design in ANSI/AISC 358-10 (2010) is based in the work of Murray and Sumner (2004).

These authors deemed negligible the contribution of the yield lines on the compression side (yield line 1).
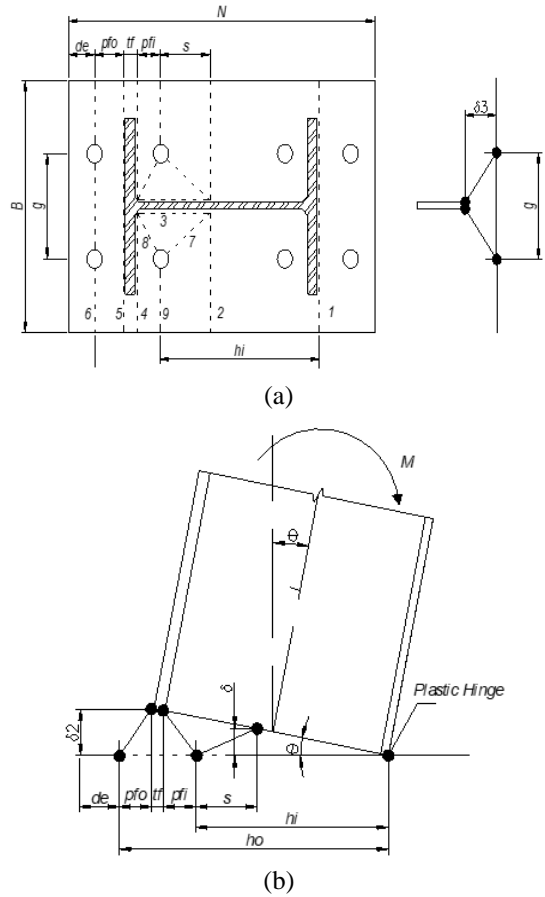

(a)

(b)

Fig. 2 (a) Plan view of Yield line patterns for EP-HSS Moment Connection and (b) Elevation view of Yield line patterns for EP-HSS Moment Connection

calculating the maximum expected moment at the face of the column induced by the beam. With this value, the thickness of the external diaphragms can be calculated by considering that they resist the bending moment through tension and compression, and that the diaphragms must remain elastic for this moment demand. The welds of the diaphragms to the HSS column are sized to resist the shear and tension induced by the bending at the face of the column. Next, the thickness of the web plate between the HSS column and the end plate (not visible in Fig. 1) and the size of the welds between this plate, the column and end-plate are calculated to resist the shear demand coming from the bending of the beam. Finally, the end-plate connection is designed. The bolts are sized to resist the moment and the shear induced by the beam. The thickness of the plate attached to the diaphragms is equal to the thickness of the beam end-plate. The beam end-plate can be sized following the recommendations for end-plate connections in ANSI/AISC 358-10 (2010). However, as part of this research, improved equations to determine the plate thickness, detailed in Section 3, are proposed, and validated

3. End-plate design

An analytical expression to calculate the capacity of the end-plate in the connection can be derived using Yield Line Theory, through virtual work. The possible mechanisms require the formation of some or all of the yield lines shown in Figs. 2(a) and 2(b). Equating the external work, done by the applied bending moment through the virtual rotation of the connection, with the internal work generated at the yield lines, the end-plate yield line mechanism parameter, *Yp*, can be determined. With *Yp*, the required thickness of the end plate, *tp, req'd*, can be calculated using equation (6.10-5) of ANSI/AISC 358-10 (2010), as will be demonstrated next.

Table 1 shows the virtual rotations and lengths of all possible yield lines for the mechanism considered, where the dimensions *g, s, pfo, pfi, ho*, and *hi* are shown in Figs. 2(a) and 2(b). In the next subsections, the expression in

Table 1 Virtual rotations (θ) and yield line lengths (l)

Yield line	Length (l_i)	Rotation (θ_i)
1	B	θ
2	B/2	$\theta(h_i/s - 1) + \theta$
3	$p_{fi} + s$	$2\theta(h_i/g)$
4	B/2	$\theta\left(\dfrac{h_i}{p_{fi}} + 1\right) - \theta$
5	B	$\theta\left(\dfrac{h_o}{p_{fo}} - 1\right) + \theta$
6	B	$\theta\left(\dfrac{h_o}{p_{fo}} - 1\right)$
7	L_7	$\dfrac{\theta h_i}{L_7}\left(\dfrac{g}{2s} + \dfrac{2s}{g}\right)$
8	L_8	$\dfrac{\theta h_i}{L_8}\left(\dfrac{g}{2p_{fi}} + \dfrac{2p_{fi}}{g}\right)$
9	$B - g/2$	$\theta\left(\dfrac{h_i}{p_{fi}} + \dfrac{h_i}{s}\right)$

They also assumed that the thickness of the base plate was enough to prevent prying. Hence, the bolt locations are considered fix points and there is no external work associated with the bolt forces. Under these assumptions, the internal virtual work done can be calculated using Eq. (1), considering only yield lines 2 through 9.

3.1 AISC 358-10 end-plate design

The flexural strength of end-plate is achieved equating the external work of the moment applied with the internal work. The virtual displacements are obtained as follow

$$\delta = \theta(d/2) \qquad (1)$$

$$\delta_2 = \theta(h_o \text{-} p_{fo}) \qquad (2)$$

$$\delta_3 = \theta(h_i) \qquad (3)$$

The internal work generated at the yield lines 2, 3, 4, 5, 6, 7, 8 and 9 is obtained as follow

$$W_I = \left(\sum_i \theta_i \, l_i \right) m_{pi} \qquad (4)$$

After substituting the values from Table 1 and simplifying algebraically, Eq. (5) is obtained

$$W_I = \theta \times m_p \left\{ B \left[2h_i \left(\frac{1}{s} \right) + \left(\frac{2h_i}{p_{fi}} \right) + \left(\frac{2h_o}{p_{fo}} \right) \text{-}1 \right] + \frac{8}{g} h_i (p_{fi} + s) \right\} (5)$$

The external work is only done by the applied moment, resulting in the expression in Eq. (6)

$$W_E = M\theta \qquad (6)$$

Equating external and internal work, Eq. (7) can be obtained to determine the moment resistance of the connection for the plastic mechanism considered.

$$M = m_p \left\{ B \left[2h_i \left(\frac{1}{s} \right) + \left(\frac{2h_i}{p_{fi}} \right) + \left(\frac{2h_o}{p_{fo}} \right) \text{-}1 \right] + \frac{8}{g} h_i (p_{fi} + s) \right\} \quad (7)$$

Since the location of the bolts is known, the only variable is the location of yield line 2. To find the minimum upper bound, Eq. (7) must be derived with respect to *s* and equated to zero, yielding the value of *s* in Eq. (11), as follow

$$\frac{\partial \left\{ 2Bh_i \left(\frac{1}{s} \right) + \frac{8}{g} h_i s \right\}}{\partial s} = 0 \qquad (8)$$

$$\text{-}2Bh_i \frac{1}{s^2} + \frac{8}{g} h_i = 0 \qquad (9)$$

$$\frac{4}{g} s^2 = B \rightarrow s = \frac{1}{2} \sqrt{gB} \qquad (10)$$

Equating *B=bp*

$$s = \frac{1}{2} \sqrt{b_p g} \qquad (11)$$

By inspecting Eq. (7), Yp can be defined by Eq. (12).

$$Y_p = \left\{ B/2 \left[h_i \left(\frac{1}{s} + \frac{1}{p_{fi}} \right) + \left(\frac{h_o}{p_{fo}} \right) \text{-} \frac{1}{2} \right] + \frac{2}{g} h_i (p_{fi} + s) \right\} \qquad (12)$$

Equating the bending moment M on the connection to M_f, the maximum moment at the face of the column, replacing mp by the plastic moment capacity of a unit length of plate, and applying the strength factor ϕ_d to the nominal strength, Eq. (15) can be obtained. Rearranging Eq. (15), the expression to calculate the required end-plate thickness given by Eq. (17) is found.

$$M = m_p \times Y_p \qquad (13)$$

$$m_p = F_y \times \frac{t_p^2}{4} \qquad (14)$$

Substituting Eq. (14) in Eq. (13)

$$M = F_y \times \frac{t_p^2}{4} \times Y_p \qquad (15)$$

$$t_p = \sqrt{4 \times M / F_y \times Y_p} \qquad (16)$$

Substituting (4xM) by (1,11M$_f$), where (1,11) is a factor to ensure thick plate behavior and avoid the prying in the end-plate. Additionally, applying the strength factor ϕ_d to the nominal strength, the flexural strength of end-plate is obtained as follow

$$t_p = \sqrt{1.11 \times M_f / \emptyset_d F_y \times Y_p} \qquad (17)$$

Eqs. (12) and (17) correspond to the expressions in AISC 358-10 (2010).

3.2 Proposed end-plate design

The modified expressions are derived considering now the contribution of yield lines 1, 2, 3, 4, 5, 6, 7, 8 and 9 to the strength of the plate. Repeating the same procedure, but including the additional strength provided by the yield line 1, an alternative *"Y$_{P\,EP-HSS}$"* parameter is obtained, as shown in Eq. (18), which optimizes the thickness of the end-plate.

$$Y_{pEP-HSS} = \left\{ b_p/2 \left[h_i \left(\frac{1}{s} + \frac{1}{p_{fi}} \right) + \left(\frac{h_o}{p_{fo}} \right) \right] + \frac{2}{g} h_i (p_{fi} + s) \right\} \quad (18)$$

The parameter calculated using Eq. (18) is larger than the parameter calculated using Eq. (12), resulting in a reduction of the required thickness of the end-plate. Numerical and experimental studies were conducted to evaluate the level of reduction of the plate thickness and the effects on the connection performance. The results of these studies are shown in Sections 4 and 5.

4. Numerical model of EP-HSS moment connection

A numerical analysis of two models of connections using the Finite Element Method (FEM) with ANSYS v14,

ANSYS (2012), was performed. The numerical study was performed considering the nonlinear characteristics of the material, geometrics nonlinearities, contact nonlinearities, and boundary conditions. Large deflections effects were considered in the simulations due to the high rotations level reached in the connections, according to Diaz (2010) and Diaz *et al.* (2011).

The first model analyzed, EP-HSS (1), was obtained from the design of the connection with the pattern of yield lines established in ANSI/AISC-358-10 (2010). An exterior joint configuration was obtained from a four-story residential building designed according to the requirements of the AISC Specifications, ANSI/AISC 360-10 (2010) and ANSI/AISC 341-10 (2010). The column plate design was controlled by the maximum expected flexural strength of the beam. Likewise, the bolts and end-plates were designed for the maximum expected flexural strength of the beam.

The design of the column was performed considering concrete filled tubes, and it was controlled by the shear force demand in the panel zone and the strong column-weak beam criteria, as well as the maximum allowed drift requirement. The welds were designed to the maximum expected tension and shear strength of connecting elements. The details of the connection are presented in Figs. 3(a)-3(c). The results of the design process are shown in Table 2 and the nominal properties of the materials for design in the Table 3. The nominal flexural strength of the beam (IPE-200) is 54.82 [kNm]. The second model analyzed, EP-HSS (2), was obtained with the same procedure according to Specification, but using the *"$Y_{P\text{-}EP\text{-}HSS}$"* parameter proposed in Section 3. The only difference with EP-HSS (1) was the thickness of the end-plates, which was 19 [mm] instead of 22 [mm].

Table 2 Dimensions of elements in EP-HSS

Member	tf [mm]	tw [mm]	d [mm]	bf [mm]	tp [mm]	t [mm]
Column: HSS 220x220x9	-	-	220	220	-	9
Beam: IPE-200	8.5	5.6	200	100	-	
End-plate	-	-	-	-	22	
Horizontal diaphragm	-	-	-	-	16	
Vertical diaphragm	-	-	-	-	8	

Table 3 Nominal material properties of steel members

Member	Designation	Yield Strength [MPa]	Ultimate Strength [MPa]
Column: HSS 220x220x9	ASTM-A-500 Gr. B	350	400
Beam: IPE-200	ASTM-A-36	250	400
End-plate, plates	ASTM-A-36	250	400

Notes: Young's modulus of all metals E = 210,000 [MPa], Poisson's ratio ν = 0.3
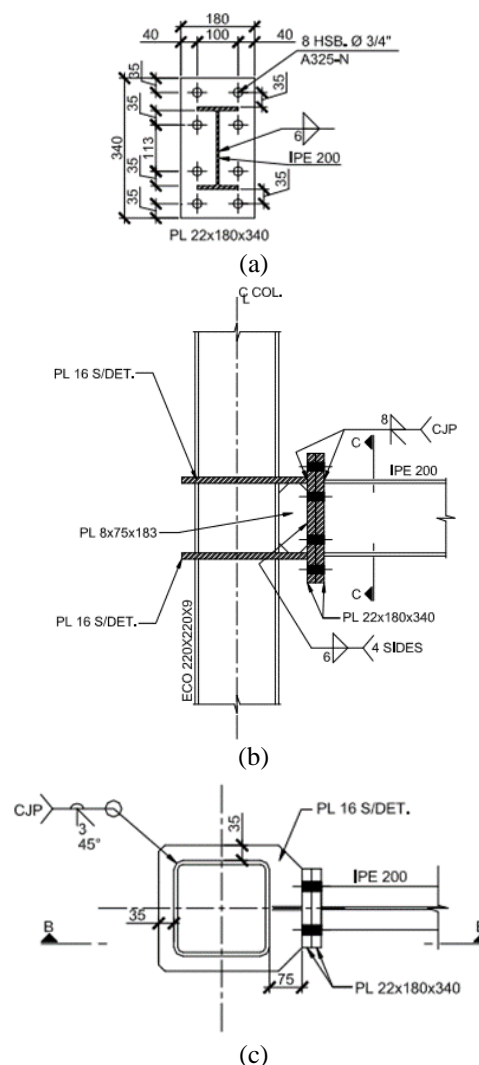

(a)

(b)

(c)

Fig. 3 (a) Details of end-plate [mm], (b) Elevation view of EP-HSS Moment Connection [mm] and (c) Plan view of EP-HSS Moment Connection [mm]

4.1 General characteristics of the numerical model

The two models analyzed with similar dimensions that experimental specimens share the following considerations:

(1) The length of the column is the story height, considering that the inflection points in the columns occur at mid-height of each story, as show in Fig. 13(b).

(2) Welds and washers are not included in the model for simplicity and to avoid convergence problems, considering that inelastic incursion is not expected in these elements.

(3) The diameter of the bolt holes is assumed equal to the diameter of the bolts, in order to avoid rigid body movements that cannot be easily handled by the software, because the kinetic energy provided by the movement cannot be compensated with the internal strain energy of the system.

4.2 Element type and mesh

The model was built using hexahedral and tetrahedral

3D solid elements (SOLID 186) for stiffeners, plates, bolts, beams, column, and nuts, to avoid potential conflicts that occur at the interface of elements of different types (PLANE, SHELL, SOLID). The SOLID186 elements can be used with materials with plasticity, hardness, yield strength, large deflections and large deformations. This element has three translational degrees of freedom per node and has 20 nodes, ANSYS (2012).

In order to obtain a better computational efficiency and fast convergence, a fine mesh is used in zones where large inelastic incursions are expected and a coarser mesh is used in other zones. The difference in mesh refinement can be seen in Fig. 4. The number of elements and nodes used in each component of the model is detailed in Table 4.

4.3 Boundary conditions, contacts and loading

The ends of the column, points A and B in Fig. 5(a), were pinned to simulate the location of the inflection points and the displacement was applied at the free end of the beam, which represents the inflection point in the beam.

The displacement history applied followed the protocol established in ANSI/AISC 358-10 (2010). The boundary conditions and displacements were applied using the "Remote Point Displacement" command. Additionally, the bolts were pretensioned to 70% of the nominal tension strength as specified in ANSI/AISC 341-10 (2010) as shown in Fig. 5(b). The load sequence of test and FEM is shown in the Table 5.

Table 4 Number of elements and nodes in FEM model

Component	EP-HSS (1) and (2)	
	Number of elements	Number of nodes
End-plate	3147	17380
Column	9152	61992
Beam	2583	18222
Bolt	336	1708
Nut	96	624
Vertical Stiffener	142	1122
Horizontal Stiffener	962	6091

Notes: EP-HSS (1) model with "Yp" Parameter and EP-HSS (2) model with "YpEP-HSS" parameter
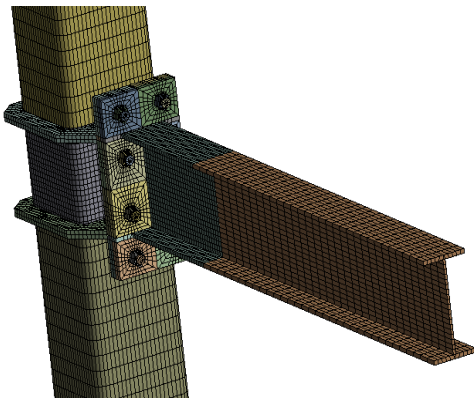

Fig. 4 Mesh of EP-HSS Moment Connection

The contact between end-plates is type "Frictional", which allows the separation between the connected elements and takes into account the friction of tangential movement between these elements. The friction coefficient was assumed as μ = 0.3, according to Diaz (2010) and Diaz *et al.* (2011). The contact between bolts and nuts was simulated using contacts type "Frictionless" which allows separation between the connected parts and allows the tangential movement without considering the friction, according to research conducted by Kim (2007).
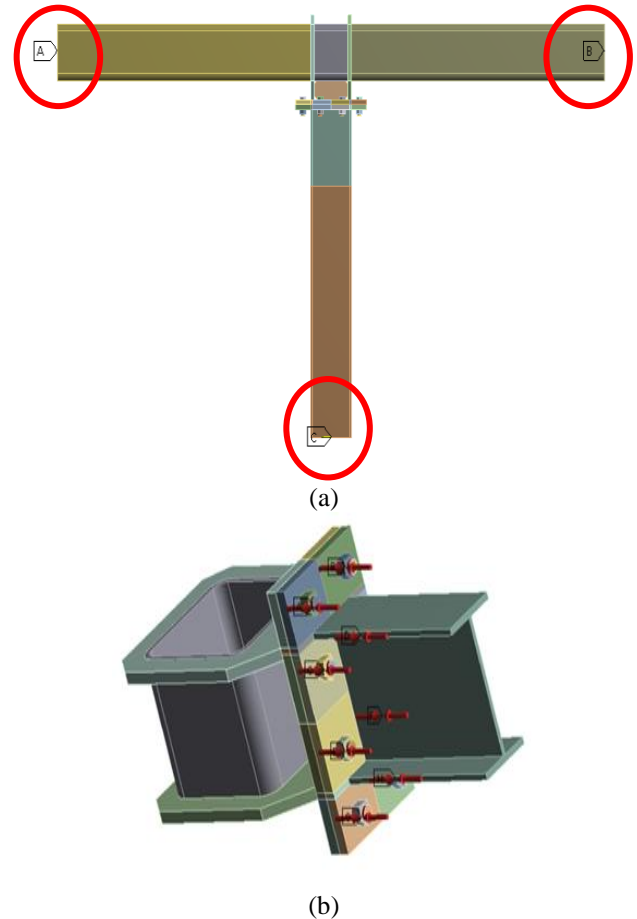

(a)

(b)

Fig. 5 (a) Boundary conditions in numerical model: "A" and "B" indicate column ends, "C" free end of beam (b) Bolt pretension in the numerical model

Table 5 Load protocol of tests and FEM

No.	No. of cycles	Drift angle (θ) [rad]
1	6	0.00375
2	6	0.005
3	6	0.0075
4	4	0.01
5	2	0.015
6	2	0.02
7	2	0.03
8	2	0.04

Note: continue loading at increments of θ=0.01 [rad], with two cycles of loading at each step

Table 6 Type of contacts used in the numerical models

Elements connection	Contact	Movement in normal direction	Movement in tangential direction
Beam-Column	Bonded	No separation	No slip
Column-Horizontal Stiffeners	Bonded	No separation	No slip
Column-Vertical Stiffeners	Bonded	No separation	No slip
Vertical Stiffeners-Horizontal Stiffeners	Bonded	No separation	No slip
End Plate-Horizontal Stiffeners	Bonded	No separation	No slip
End Plate-Vertical Stiffeners	Bonded	No separation	No slip
End Plate-End plate	Frictional	Separation allowed	Slip allowed
Beam-End plate, Bolt-Nut	Bonded	No separation	No slip
Bolt- End plate, Nut-End plate	Frictionless	Separation allowed	Slip allowed

A contact type "Bonded" was used for the connections between end-plate and beam, end-plate and horizontal and vertical diaphragms, and horizontal and vertical diaphragms and column, which prevents relative movement between the parts in contact, simulating the effect of the welds. Table 6 summarizes the contacts before mentioned.

4.4 Material modeling

The FEM used different steel types for beams, columns, vertical and horizontal stiffeners, and bolts. The steel stress-strain relationships are defined in multi-linear form. A multi-linear kinematic hardening rule with von-Mises yielding criterion was used to simulate metal plasticity. Additionally, actual material properties from tensile tests were converted and idealized to true stress and true strain values which were used as input for the FEM models. The material properties are shown in Table 7 and the stress-strain curves used in the FEM model for the beam, the bolts and the column are shown in Figs. 6-8 respectively.

Table 7 Material properties from tensile specimen

Element	Designation	σy [MPa]	εy [mm/mm]	σu [MPa]	εu [mm/mm]
Beam, Stiffeners, End-plates	ASTM-A-36	380	0.0018	575	0.20
Column	ASTM-A-500 Gr. B	496	0.0025	597	0.01
Bolt	ASTM-A-325	634	0.0036	848	0.14

Notes: (σy), Yield stress, (εy), Yield strain, (σu), Ultimate stress, (εu), Ultimate strain
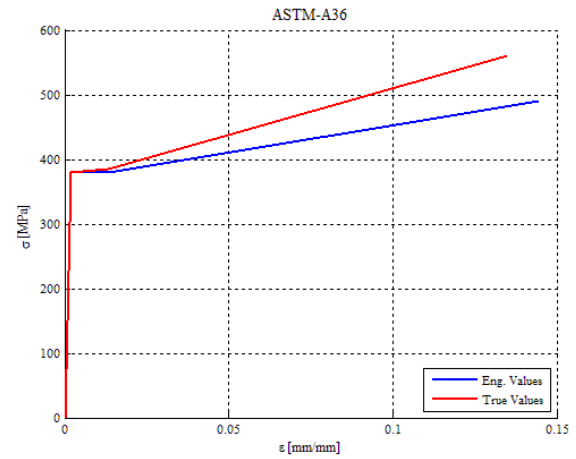

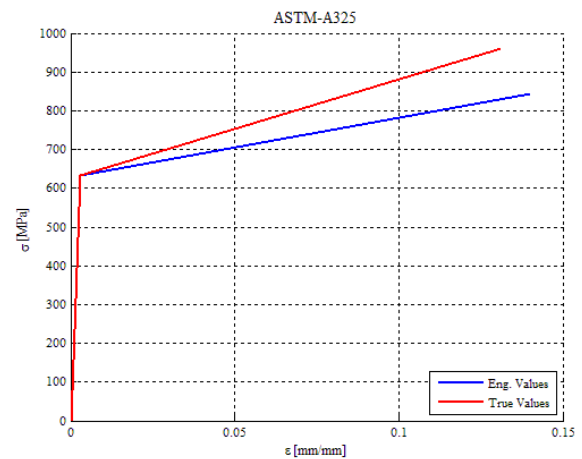Fig. 6 Material model true stress and true strain curve for ASTM-A-36

Fig. 7 Material model true stress and true strain curve for ASTM-A-325

4.5 Results of FEM models

According to ANSI/AISC 341-10 (2010), the story drift angle of beam to column connections used in the seismic force system should accommodate at least 0.04 [rad], and the flexural resistance of the connection determined at the column face should be at least $0.80M_p$ at a story drift angle of 0.04 [rad]. Additionally, the failure mechanism should be controlled by plastic hinges in the beams, considering a strong-column weak-beam mechanism for seismic design. The results of the numerical study are shown for EP-HSS (1) and EP-HSS (2), in terms of load-displacement, moment-rotation hysteresis and secant-stiffness curves. Additionally, the von-Mises equivalent stress distribution and plastic deformations at the point of maximum load are presented.

4.5.1 Results of EP-HSS (1) model

The connection model EP-HSS (1) reached a maximum load of 66.14 [kN], a flexural strength of 1.8 times the nominal flexural strength of the beam, and a maximum drift of 0.05 [rad], as shown in Figs. 9(a) and 9(b). In addition, an adequate performance in the connection was observed, with inelastic incursion of the beam, as shown by the hysteretic cycles where there is no evidence of brittle failure mechanisms.

The hysteretic cycles exhibit degradation of stiffness relative to initial stiffness of 2% up to 0.01 [rad] and 54% at 0.04 due to the inelastic incursion of the beam, shown in Fig. 9(c). As shown in Figs. 10(a)-10(d), a stress concentration in the beam, above the expected yielding values and deformations were obtained. In addition, the column and the connection elements do not experience inelastic incursions.

4.5.2 Results of EP-HSS (2) model

The connection model EP-HSS (2) reached a maximum load of 66.46 [kN], a flexural strength of 1.82 times the nominal flexural strength of the beam, and a maximum drift of 0.05 [rad], as shown in Figs. 11(a) and 11(b). Again, adequate performance of the connection was observed, with inelastic incursion of the beam, as shown by the hysteretic cycles where there is no evidence of brittle failure mechanisms, and the connection elements remaining elastic.

In addition, hysteretic cycles exhibited stable stiffness reaching a degradation of 16% at 0.01 [rad].

A degradation of 56% of the secant stiffness is achieved at 0.04 [rad] due to the inelastic incursion of the beam, shown in Fig. 11(c). As shown in Figs. 12(a)-12(d), a stress concentration in the beam, above the expected yielding values and deformations exceeding the elastic limits are obtained. Similarly, the column and the connection elements do not experience inelastic incursions.
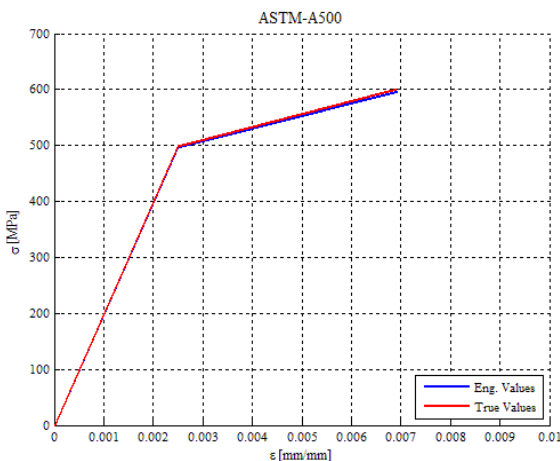

(a)

(b)

(c)

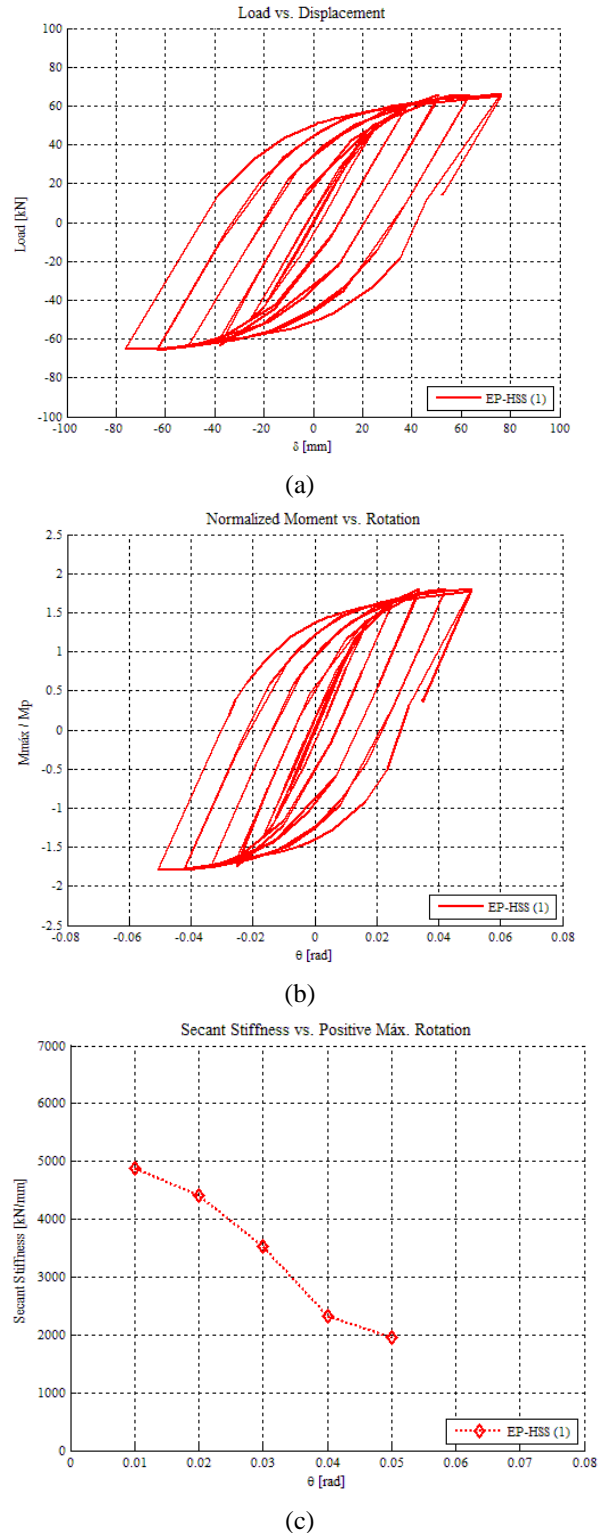Fig. 8 Material model true stress and true strain curve for ASTM-A-500 Gr. B

Fig. 9 (a) Load -Displacement Hysteresis curve of EP-HSS (1), (b) Normalized Moment-Rotation Hysteresis curve of EP-HSS (1) and (c) Secant Stiffness-Maximum Positive Rotation curve of EP-HSS (1)
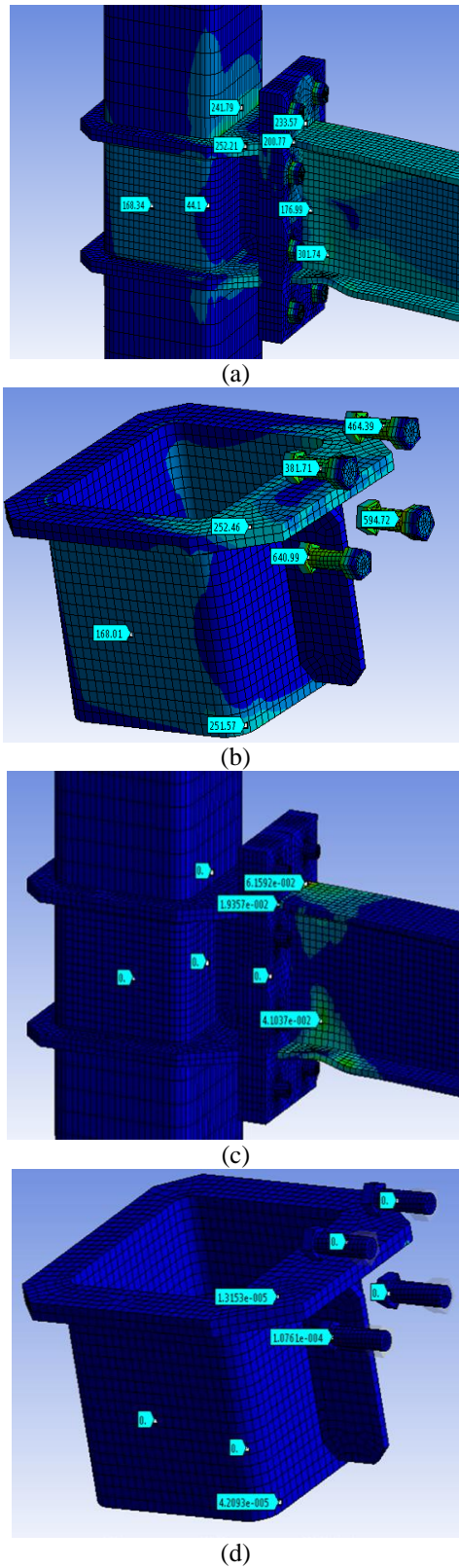
(a)

(b)

(c)

(d)

Fig. 10 (a) Distribution of von Mises stress at the maximum load of EP-HSS (1)in [MPa], (b) Distribution of von Mises stress at the maximum load of EP-HSS (1) in [MPa], (c) Plastic deformations at the maximum load of EP-HSS (1) in [mm/mm] and (d) Plastic deformations in internal elements at the maximum load of EP-HSS (1) in [mm/mm]
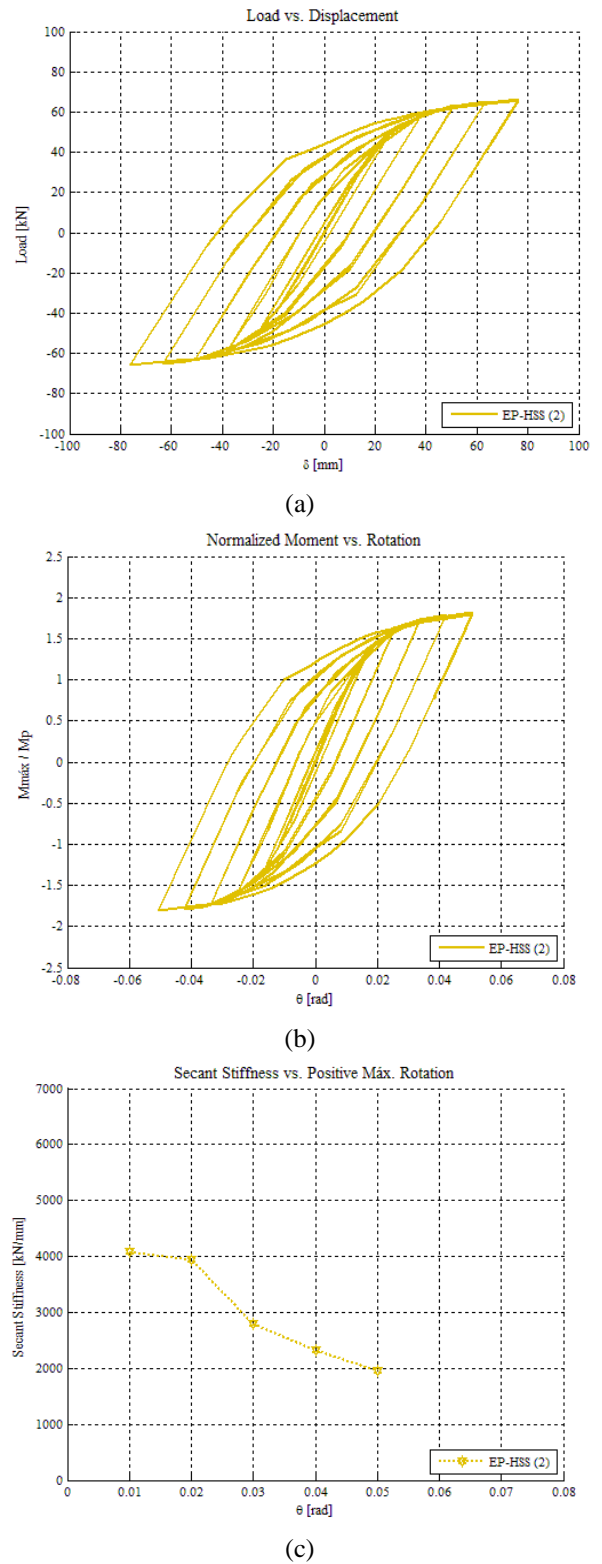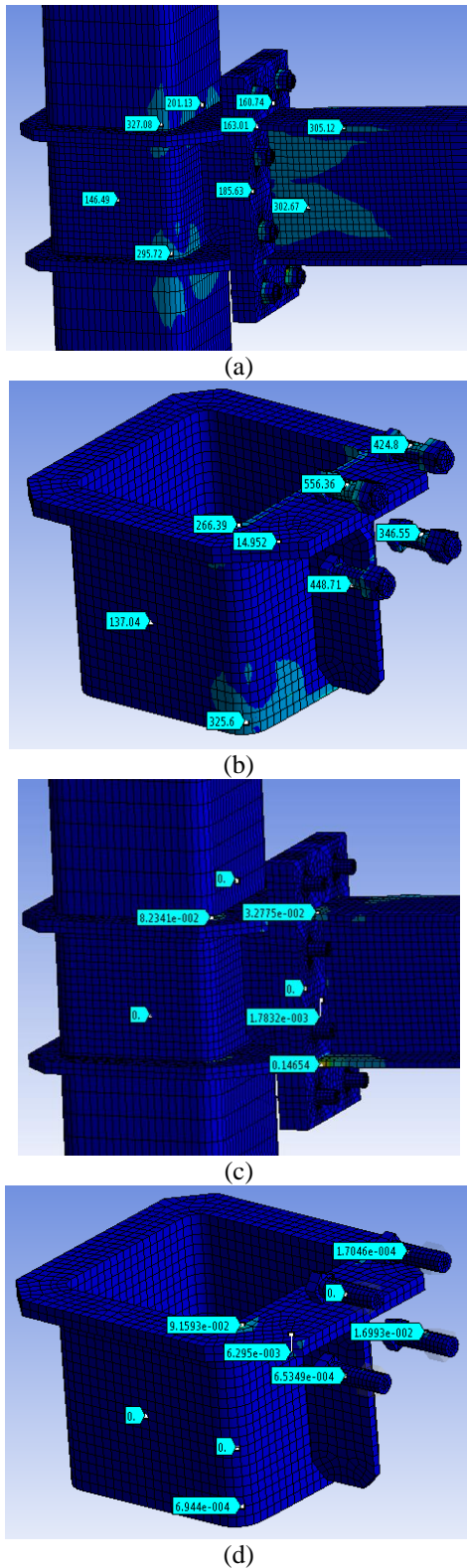

(a)

(b)

(c)

Fig. 11 (a) Load -Displacement Hysteresis curve of EP-HSS (2), (b) Normalized Moment-Rotation Hysteresis curve of EP-HSS (2) and (c) Secant Stiffness-Maximum Positive Rotation curve of EP-HSS (2)

(a)

(b)

(c)

(d)

Fig. 12 (a) Distribution of von Mises stress at the maximum load of EP-HSS (2) in [MPa], (b) Distribution of von Mises stress at the maximum load of EP-HSS (2) in [MPa], (c) Plastic deformations at the maximum load of EP-HSS (2) in [mm/mm] and (d) P Plastic deformations in internal elements at the maximum load of EP-HSS (2) in [mm/mm]

5. Experimental study of EP-HSS moment connection

Three large-scale specimens were tested to evaluate the effect of the end-plate thickness reduction on the connection performance. The specimens were all equal to EP-HSS (1), in order to ensure repeatability of the results. The as-measured material properties were already presented in Table 7. The instrumentation consisted of 3 LVDT (linear variable differential transducers) that capture the displacements of interest and one load cell to record the applied load.

LVDT-1 was located in the actuator positioned in the end of the beam to capture the displacement applied, while LVDT-2 and LVDT-3 were located at the end of the columns to verify if there was any movement, as indicated in Figs. 13(a) and 13(b). The actuator load capacity was 500 [kN] with a maximum displacement range of ±125 [mm]. The force transducer, model 661.23F -01 SN: 0375349 manufactured by MTS Systems Corporation USA, was mounted on the actuator.

The displacement applied by the actuator was as indicated in ANSI/AISC 341-10 (2010), detailed in Table 5.
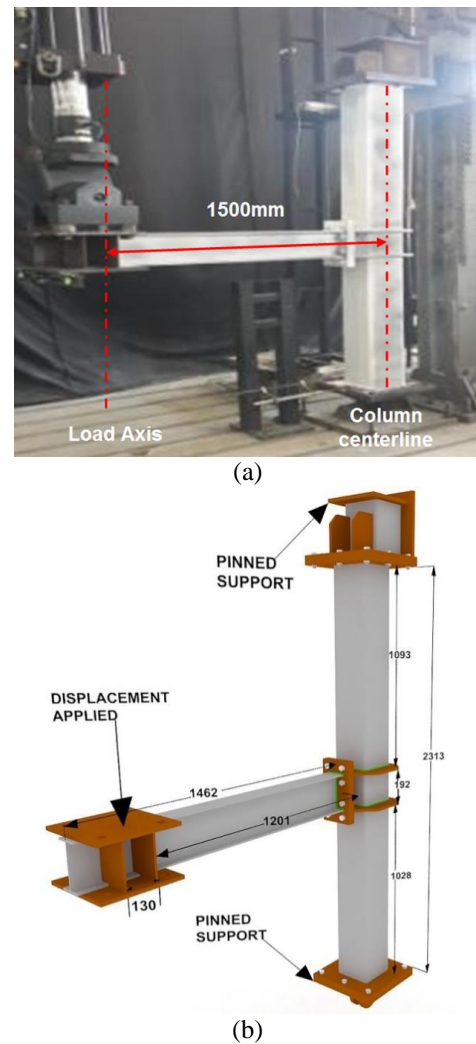

(a)

(b)

Fig. 13 (a) Test assembly and (b) Geometry and dimensions of EP-HSS (1) specimens in [mm]

5.1 Experimental results
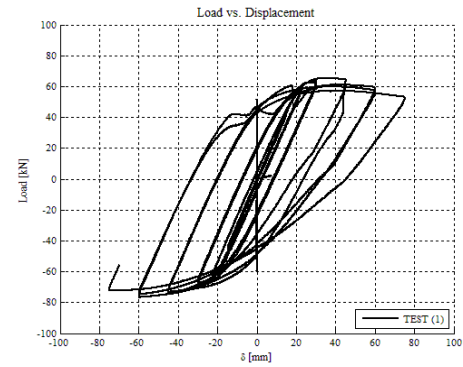
In the experimental study, the results show the following: Specimen 1 reached a maximum load of 65.26 [kN], 1.79 times the nominal flexural resistance of the beam, and a maximum drift of 0.06 [rad], as shown in Fig. 14a-14b-14c-14d-14e. The hysteretic cycles exhibited stiffness stable reaching a degradation of 8% of the initial elastic stiffness at 0.01 [rad]. A stiffness degradation of 65% is observed at 0.04 [rad], due to inelastic incursion of the beam. The column and connection elements do not experience inelastic incursions, being only the beam where all inelastic action is concentrated, showing a ductile failure. The initial disturbance visible in the response curves of Specimen 1 shows an, due to decoupling of a mechanical element of the setup during the test, which was solved without major problems for the rest of the test and subsequent tests.

Specimen 2, reached a maximum load of 71.90 [kN], 1.97 times the nominal flexural resistance of the beam, and a maximum drift of 0.05 [rad], as shown in Figs. 15(a)-15(e). The hysteretic cycles exhibited stable stiffness reaching a degradation with respect to the initial elastic stiffness of 13% at 0.01 [rad]. A 64% secant stiffness degradation was observed at 0.04 [rad], due to inelastic incursion of the beam. The column and connection elements did not experience inelastic incursions, being only the beam where all inelastic action is concentrated, achieving a ductile failure.

Specimen 3, reached a maximum load of 70.70 [kN], 1.93 times the nominal flexural resistance of the beam, and a maximum drift of 0.05 [rad], as shown in Fig. 16a-16b-16c-16d-16e. A stiffness degradation of 5% with respect to the initial elastic stiffness was observed at 0.01 [rad], and of 60% at 0.04 [rad]. The column and connection elements did not experience inelastic incursions, being only the beam where all inelastic action is concentrated, showing a ductile failure. This desirable performance, as per the seismic design philosophy, was achieved in all three specimens, showing promise of its suitability for Moment Connections in Special Moment Frames.
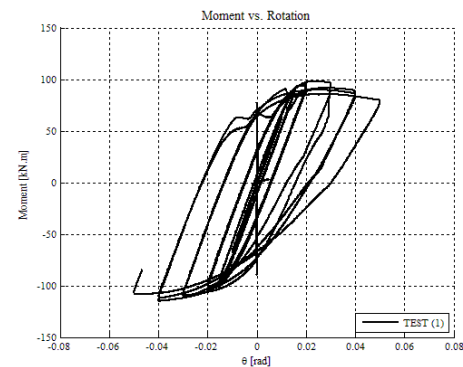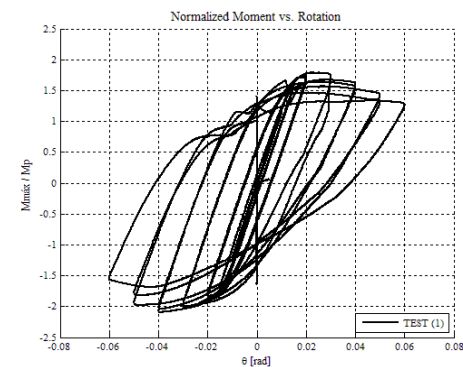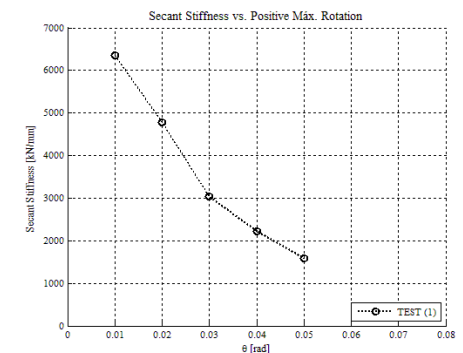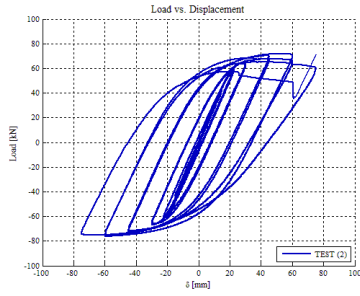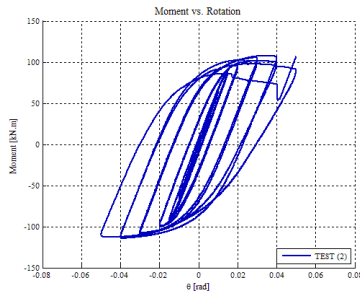
(a)
Continued-

(b)

(c)

(d)

(e)

Fig. 14 (a) View of damage in test 1, (b) Load - Displacement Hysteresis curve in test 1, (c) Moment-Rotation Hysteresis curve in test 1, (d) Normalized Moment-Rotation Hysteresis curve in test 1 and (e) Secant Stiffness-Maximum Positive Rotation curve in test 1
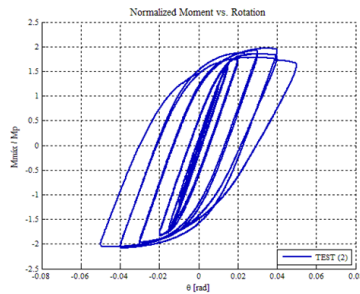
Fig. 15 (a) View of damage in test 2, (b) L Load - Displacement Hysteresis curve in test 2, (c) Moment-Rotation Hysteresis curve in test 2, (d) Normalized Moment-Rotation Hysteresis curve in test 2 and (e) Secant Stiffness-Maximum Positive Rotation curve in test 2
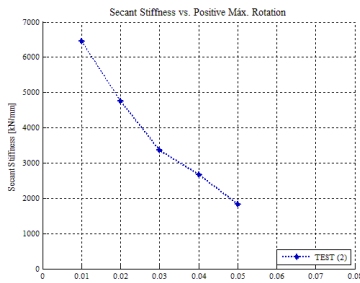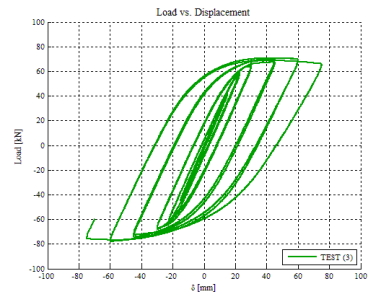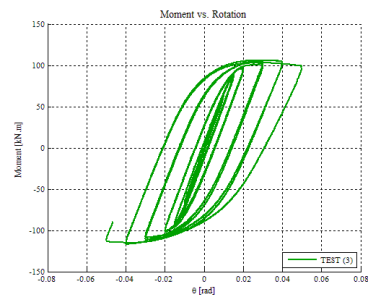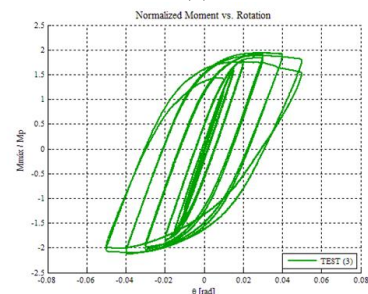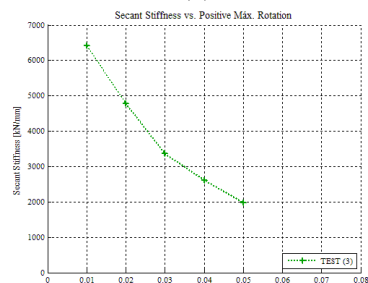
Fig. 16 (a) View of damage in test 3, (b) Load - Displacement Hysteresis curve in test 3, (c) Moment-Rotation Hysteresis curve in test 3, (d) Normalized Moment-Rotation Hysteresis curve in test 3 and (e) Secant Stiffness-Maximum Positive Rotation curve in test 3

6. Comparison of FEM and experimental results

Table 8 shows the ratio between the maximum moment reached and the expected moment and 80% of the nominal plastic moment of the beam, $M_n=FyZx=54.82$ [kNm], showing that both models in FEM and the specimens tested reached a flexural resistance greater than nominal plastic moment and comply with the requirements of AISC Specifications, ANSI/AISC 360-10 (2010), ANSI/AISC 341-10 (2010) and ANSI/AISC 358-10 (2010). In the table 9 are resumed the values obtained in FEM and tests.

As shown in Figs. 17(a) and 17(b), a repeatability of the tests was obtained, with a slightly lower stiffness and strength observed for Specimen 1. The flexural resistance largely exceeded the requirements established by the protocol qualification of ANSI/AISC 341-10 (2010). The FEM models show a similar performance regardless of the thickness of the end plate, therefore the improved equations to determine this value can be used without detriment to the specimen performance. Also, from Figs. 17(a) and 17(b), the experimental and FEM responses can be compared.

The model captures the stiffness properly, with slight differences due to the additional flexibilities induced by the test setup, which are not modeled. The FEM models achieve similar flexural resistance at 0.04 [rad] drift and maximum rotation than the experiments, but they are not capable of capturing adequately the full strength and its degradation, thereby generating differences in terms of the energy dissipated for the same drift level.

Table 8 Comparison of flexural strength between numerical and experimental specimens

Connection specimen	M / Mpe	M / 0.8Mp
EP-HSS (1)	1.21	2.26
EP-HSS (2)	1.21	2.27
Test 1	1.19	2.23
Test 2	1.31	2.46
Test 3	1.29	2.42

Notes: (M) Moment obtained, (Mp) Plastic moment and (Mpe) Expected plastic moment

Table 9 Summary of maximum values obtained in tests and FEM

Connection specimen	ML [kN]	MD [mm]	IS [kN/mm]	DE [N.m]	MM [kN.m]	MR [rad]
EP-HSS (1)	66.14	76	4979	40532	99.20	0.05
EP-HSS (2)	66.46	76	4844	36171	99.69	0.05
Test 1	65.26	90	6933	58140	97.89	0.06
Test 2	71.90	75	7451	44126	107.85	0.05
Test 3	70.70	75	6519	53543	106.05	0.05

Notes: (ML) Maximum load, (MD) Maximum displacement, (IS) Initial stiffness, (DE) Dissipated energy, (MM) Maximum moment obtained and (MR) Maximum rotation obtained
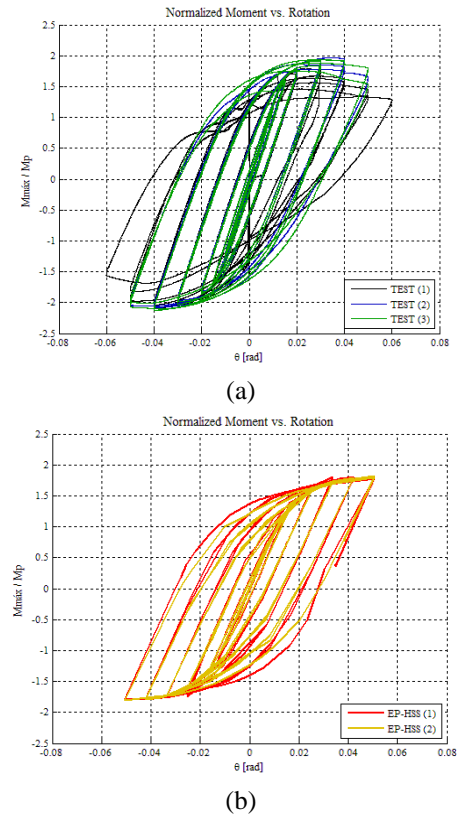

(a)

(b)

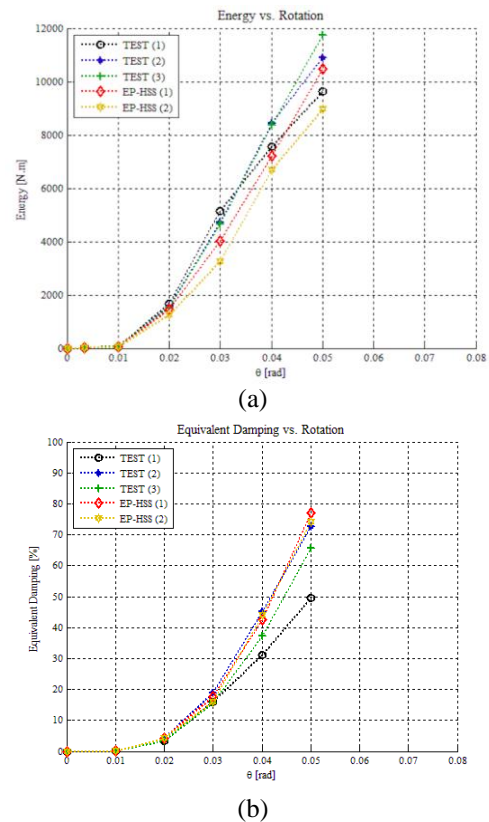Fig. 17 (a) Experimental results and (b) Numerical results

(a)

(b)

Fig. 18 (a) Comparison of dissipated energy between tests and FEM models and (b) Comparison of equivalent damping between tests and FEM models

The energy dissipated was obtained for the test specimens and the numerical models and the results are shown in Fig. 18(a). The energy dissipated in the tests is larger than the energy dissipated in the FEM model analyses. In particular, Specimens 1, 2, and 3 dissipate 1.6, 1.2 and 1.5 times more energy than EP-HSS (2), respectively. On average, the tested specimens dissipated 1.36 times more energy than the corresponding FEM model, because the specimens tested had a higher capacity for the same level of deformation.

The Equivalent viscous damping results are shown in Fig. 18(b), observing an increase with increasing rotation, showing a similar trend between the specimens tested and the FEM models. Additionally, a low level of damping is observed up to a rotation of 0.01 [rad], increasing exponentially from there to damping values over 30% at 0.04 [rad], which reflects the relationship between the level of damage and the energy dissipated.

7. Conclusions

A new type of moment connection between WF beams and HSS columns was proposed, which can be welded in the shop and bolted in the field. The proposal included a revision of the formulas used to calculate the minimum required thickness of the end plate and an improved equation to determine this value. Numerical simulations using FEM for connections using the conventional ANSI/AISC 358-10 (2010) end plate thickness calculation for EP-HSS (1) and the proposed equation for EP-HSS (2) were performed, showing that the performance was satisfactory in both cases, reaching a flexural resistance above 1.8 times of the nominal flexural resistance of the beam and a rotation capacity of 0.05 [rad].

Failure concentrated on the beam, while the column and connection remained elastic, complying with the seismic design philosophy where the beam is the fuse element in connections for Special Moment Frames. It was verified numerically for the configuration analyzed, that it is possible to consider an alternative failure pattern for the end plate, which allows a thickness reduction of 16% for the end plate, without hampering the connection performance.

Full-scale specimens of three specimens similar to the EP-HSS (1) moment connection were performed, obtaining an adequate performance, where resistance exceeded on average 1.9 times the nominal flexural resistance of the beam and drifts in excess of 0.04 [rad] were achieved. No brittle failure mechanism associated with the column, plates, stiffeners, or bolts was observed. All inelastic action occurred in the beam, where only after 0.04 [rad] local buckling in flanges and webs was observed.

Additionally, the column remained elastic for the maximum deformation of the specimens. The energy dissipated increased as rotation cycles reached larger amplitudes in both the FEM models and the tested specimens. Equivalent viscous damping followed the same trend, with values below 2% for rotations up to 0.01 [rad]. From there, damping increased exponentially to values above 30% for 0.04 [rad].

References

ANSI/AISC 341-10 (2010), Seismic provisions for structural steel buildings, American Institute of Steel Construction, Chicago, IL, USA.

ANSI/AISC 358-10 (2010), Prequalified connections for special and intermediate steel moment frames for seismic applications, American Institute of Steel Construction, Chicago, IL, USA.

ANSI/AISC 360-10 (2010), Specification for structural steel buildings, American Institute of Steel Construction, Chicago, IL, USA.

ANSYS (2012), ANSYS. Theory reference, ANSYS Inc., Canonsburg, PA, USA.

Ataollahi, S. and Banan, M. (2016), "Numerical cyclic behavior of T-RBS: A new steel moment connection", *Steel Compos. Struct.*, **21**(6), 1251-1264.

Čermelj, B. and Beg, D. (2014), "Cyclic behavior of welded stiffened beam-to-column joints — experimental tests", *Steel Constr.*, **7**(4), 221-229.

Čermelj, B., Može, P. and Sinur, F. (2016), "On the prediction of low-cycle fatigue in steel welded beam-to-column joints", *J. Constr. Steel Res.*, **117**, 49-63.

Díaz, C. (2010), "Diseño de uniones semirrígidas mediante simulación numérica y modelos Kriging", Doctoral Dissertation (in Spanish), Universidad Politécnica de Cartagena, Spain.

Díaz, C., Victoria, M., Martí, P. and Querin, O.M. (2011), "FE model of beam-to-column extended end-plate joints", *J. Constr. Steel Res.*, **67**(10), 1578-1590.

Esfandyary, R., Razzaghi, M. and Eslami, A. (2015), "A parametric investigation on the hysteretic behavior of CFT column to steel beam connections", *Struct. Eng. Mech.*, **55**(1), 205-228.

Fadden, M. (2013), "Cyclic Bending Behavior of Hollow Structural Sections and Their Application in Seismic Moment Frame Systems", Ph.D. Dissertation, University of Michigan, Ann Arbor, MI, USA.

Fadden, M. and McCormick, J. (2014a), "Finite element model of the cyclic bending behavior of hollow structural section beam members", *J. Constr. Steel Res.*, **94**, 64-75.

Fadden, M. and McCormick, J. (2014b), "HSS-to-HSS seismic moment connection performance and design", *J. Constr. Steel Res.*, **101**, 373-384.

Faridmehr, I., Osman, M., Tahir, M., Nejad, A. and Hodjati, R. (2015), "Seismic and progressive collapse assessment of SidePlate moment connection system", *Struct. Eng. Mech.*, **54**(1), 35-54.

FEMA (2000a), "Recommended seismic design criteria for new steel moment-frame buildings (FEMA-350)", Federal Emergency Management Agency, Washington, D.C., USA.

FEMA (2000b), "State of the art report on past performance of steel moment-frame buildings in earthquakes (FEMA-355E)", Federal Emergency Management Agency, Washington, D.C., USA.

Gholami, M., Deylami, A. and Tehranizadeh, M. (2013), "Seismic performance of flange plate connections between steel beams and box columns", *J. Constr. Steel Res.*, **84**, 36-48.

Kim, T.S. and Kuwamura, H. (2007), "Finite element modeling of bolted connections in thin-walled stainless steel plates under static shear", *Thin-Walled Struct.*, **45**(4), 407- 421.

Murray, T.M. and Sumner, E.A. (2004), End-Plate Moment Connections – Wind and Seismic Applications, Design Guide Series 4 – 2nd Edition, American Institute of Steel Construction, Chicago, IL., USA.

Saleh, A., Zahrai, S. and Mirghaderi, S. (2016), "Experimental study on innovative tubular web RBS connections in steel MRFs with typical shallow beams", *Struct. Eng. Mech.*, **57**(5), 785-808.

Seek, M.W. and Murray, T.M. (2008), "Seismic strength of moment end-plate connections with attached concrete slab",. *Proceedings of the Connections VI*, Chicago, IL, USA, June.

Swanson J.A. and Leon R.T. (2000), "Bolted steel connections: tests on T-stub components", *J. Struct. Eng.*, **126**(1), 50-56.

Swanson, J.A. and Leon, R.T. (2001), "Stiffness modeling of bolted T-stub connection components", *J. Struct. Eng,*, **127**(5), 498-505.

Tahir, M., Juki, I., Ishak, M. and Plank, R. (2014), "Performance of partial strength connection connected by thick plate between column flanges", *Struct. Eng. Mech.*, **51**(2), 215-228.

Yang, C., Yang, J.F., Su, M.S. and Liu, C.Z. (2016), "Numerical study on seismic behaviors of ConXL biaxial moment connection", *J. Constr. Steel Res.*, **121**, 185-201.

BU

Abbreviations

Symbol	Definition
b_f	Flange width of the beam
bp	Width of end plate
B	Width of end plate
d	Overall depth of beam
d_e	Column bolt edge distance
F_y	Specified minimum yield stress of the yielding element
g	Horizontal distance (gage) between fastener lines
h_i	Distance from centerline of compression flange to the centerline of the ith tension bolt row
h_o	Distance from centerline of compression flange to the tension-side outer bolt row in EP-HSS moment connection
l_i	length of yield line
m_p	plastic momento of beam
m_{pi}	plastic moment internal of beam
M	Moment obtained
M_f	Probable maximum moment at face of column
M_n	Nominal flexural strength of beam
M_p	Plastic moment of beam
M_{pe}	Plastic moment of beam based on expected yield stress
N	Length of end plate
p_{fi}	Vertical distance from inside of a beam tension flange to nearest inside bolt row
p_{fo}	Vertical distance from inside of a beam tension flange to nearest outside bolt row
s	Distance from centerline of most inside or most outside tension bolt row to the edge of a yield line pattern
t_f	Thickness of beam flange
t	Thickness of column
t_p	Thickness of end-plate
$t_{p, req'd}$	Thickness required of end-plate
t_w	Thickness of beam web
W_E	External work
W_i	Internal work
Y_p	End-plate yield line mechanism parameter
$Y_{p\,EP\text{-}HSS}$	End-plate yield line mechanism parameter for EP-HSS
δ	Virtual displacement for yield line 2 (Fig. 2b)
δ_2	Virtual displacement for yield line 5 (Fig. 2b)
δ_3	Virtual displacement for yield line 3,7 and 8 (Fig. 2a)
ε_u	Ultimate deformation
ε_y	Yielding deformation
ϕ_d	Resistance factor for ductile limit states
θ	Rotation angle due to moment of beam
θ_i	Rotation internal
σ_u	Ultimate stress
σ_y	Yielding stress